Transp Porous Med (2012) 92:119–143
DOI 10.1007/s11242-011-9894-7

Modeling Concentration Distribution and Deformation During Convection-Enhanced Drug Delivery into Brain Tissue

Karen H. Støverud · Melanie Darcis · Rainer Helmig · S. Majid Hassanizadeh

Received: 10 May 2011 / Accepted: 8 October 2011 / Published online: 25 October 2011

Abstract Convection-enhanced drug delivery is a technique where a therapeutic agent is infused under positive pressure directly into the brain tissue. For predicting the final concentration distribution and optimizing infusion rate and catheter placement, numerical models can be of great help. However, despite advances in modeling this process, often the infused agent does not reach the targeted region prescribed in the modeling phase. In this study, patient-specific brain structure and parameters, obtained from diffusion tensor imaging (DTI), are implemented in a numerical model which describes the flow and transport in an elastic deformable matrix. To our knowledge, this is the first time that information from DTI is used in a numerical model which includes both transport of a therapeutic agent and tissue deformation. Fractional anisotropy (FA) is used to distinguish between gray and white matter and tortuosity to differentiate between inside and outside the brain tissue. One voxel in the DT-image is represented by one element of the numerical grid. The DT-images were in addition used to determine the orientation of the white matter fiber tracts and calibrate permeability and diffusion coefficients found in the literature. Values chosen for the porosity and Lamé parameters are also based on those found in the literature. Given realistic literature values, the calibration of the permeability and diffusion tensors are shown to be successful. Our result shows that preferential flow occur in direction of the white matter fiber tracts. The current model assumes linear deformation, corresponding to small porosity changes.

K. H. Støverud (✉)
Center for Biomedical Computing, Simula Research Laboratory, Lysaker, Norway
e-mail: karenhes@simula.no

M. Darcis · R. Helmig
Department of Hydromechanics and Modeling of Hydrosystems, University of Stuttgart, Stuttgart, Germany
e-mail: Melanie.Darcis@iws.uni-stuttgart.de

R. Helmig
e-mail: Rainer.Helmig@iws.uni-stuttgart.de

S. M. Hassanizadeh
Environmental Hydrogeology, Utrecht University, Utrecht, The Netherlands
e-mail: hassanizadeh@geo.uu.nl

But, because large porosity changes occur that may adversely affect drug transport, non-linear deformations should be included in the future.

Keywords Convection-enhanced delivery · Poro-elasticity · Diffusion tensor imaging · Brain tissue

1 Introduction

1.1 Motivation

Parkinson, Alzheimer, epilepsy, and malignant brain tumors are all diseases affecting the central nervous system (CNS). In most cases, these diseases have severe consequences for the patients and the need for effective treatment is urgent. Although there often exist agents capable of curing these diseases, most therapeutic agents have proven inefficient when given orally or intravascularly. This is mainly because of two different effects. First, when one injects a therapeutic agent intravascularly it gets diluted. Thus, one needs a high dose to get the required concentration in the targeted region. But, the dose is limited by the drug concentration that the body as a whole can stand without severe consequences. Second, the blood–brain barrier (BBB) prevents many macromolecules from entering the interstitial space, which means that the drugs never reach the targeted region (Groothuis 2000).

Thus, after finding an effective therapeutic agent, the challenge is to get the agent in the right concentration to the targeted region. To overcome the problems associated with the BBB and systemic toxicity, therapeutic agents can be introduced directly into the brain tissue. This can be done by continuously infusing the agent into the brain tissue via catheters, such that a pressure gradient arises. This technique is called convection-enhanced drug delivery (CED) since the spreading is dependent on the infusion pressure and not diffusion only (Morrison et al. 1994). The pressure gradient induces flow and results in a higher concentration of the drug farther away than in the case of only diffusion-driven delivery (Raghavan et al. 2006; Morrison et al. 1994).

CED is still on an experimental level and many questions are left open. In particular, it is difficult to predict spatial distribution and local concentration variations (Raghavan et al. 2006; Groothuis 2000). One reason is that the distribution of the agent is heavily dependent on factors such as heterogeneities in the brain tissue and local differences in interstitial pressure due to edema.

Several models describing CED have already been developed and can be divided into two main categories, based on whether the CNS is described as a rigid or an elastic porous medium.

1.1.1 Rigid Models

CED was first proposed in the beginning of the 1990s and one of the first mathematical models was developed by Morrison et al. (1994). This model describes the transport of macromolecules, assuming isotropic and homogeneous brain tissue for the case of high-flow and low-flow infusion. In the latter case, they only considered diffusion. The model was based on a model by Baxter and Jain (1989) applied for low-flow infusion. Both of these models were based on analytical solutions. Later, numerical solutions were obtained for more realistic cases. For example, Raghavan et al. (2006) and Linninger et al. (2008a,b) all modeled CED into a human brain, while Sarntinoranont et al. (2003, 2006) and Kim et al. (2009, 2010) modeled CED into the spinal cord and corpus callosum of a rat. These models all used a

rigid geometry based on MR-images and both anisotropy and heterogeneities were taken into account.

1.1.2 Elastic Models

The assumption of rigidity is actually not applicable to brain tissue. So, some models use the poro-elastic theory developed by Biot (1955) to describe fluid transport in the interstitial space. Several models treating the brain as an elastic porous medium can be found in the literature. Basser (1992), Netti et al. (1997), Chen et al. (2002), and Smith and Humphrey (2007) all used a poro-elastic consolidation model and derived analytical solutions for the pressure field and velocity distribution during infusion into the center of a spherical tumor. Netti et al. (1995), Kalyanasundaram et al. (1997), Gillies et al. (2005), and Chen and Sarntinoranont (2007) used a similar poro-elastic consolidation model, but instead of deriving analytical solutions, the equations were solved numerically.

The mechanical properties of the brain and spinal cord are known to be non-linear and strain-rate-dependent (Miller and Chinzei 2002; Cheng and Bilston 2007). To account for this, Smith and Garcia (2009, 2011) recently developed a hyperelastic model. They considered two different cases: a constant pressure infusion (Garcia and Smith 2009) and a constant infusion rate (Smith and Garcia 2009). Later, they included transport of a dissolved therapeutic agent in the model (Smith and Garcia 2011). This hyperelastic model assumes a homogeneous and isotropic spherical geometry. Hyperelastic and viscoelastic models with realistic geometries have been developed to study, e.g., the pathogenesis of hydrocephalus (Taylor and Miller 2004; Dutta-Roy et al. 2008), but to our knowledge none of these models describe mass transport or include heterogeneities and anisotropy of the brain tissue.

In order to find a compromise between describing the complex structure of the brain tissue and taking into account the relevant physical processes, this study shows a workflow from MRI measurements to a computational model with realistic parameters.

1.2 Outline

The aim of this study is to combine patient-specific parameters and brain structure with a poro-elastic model. Information about the structures of the tissue is obtained from DTI and the effect of heterogeneities and anisotropy on the final concentration distribution. To our knowledge this is the first numerical model using information from DTI which includes both transport of a therapeutic agent and tissue deformation.

In Sect. 3, CED-induced flow and transport processes are described. Then, the mathematical model is presented. In Sect. 4, the determination of effective model parameters on the basis of a MRI-data set is described. Parameters that cannot be obtained from MRI are taken from the literature. Next simulations are done for the isotropic and homogeneous case and a comparison between rigid and poro-elastic models is conducted. Finally, the patient-specific parameters and brain structure are implemented and the effect of the location of the infusion is investigated. The article is concluded with a summary and a conclusion.

2 The Brain Tissue

Together with the spinal cord, the brain makes up the central nervous system (CNS). Although this is an extremely complicated system, the tissue mainly consists of two cell types; neurons and glial cells.

One can distinguish two different types of brain tissues, namely, white matter and gray matter. Gray matter has a high density of tightly packed neuron cell bodies, whereas white matter mainly consists of long axons that form fiber tracts. The outer part of the brain tissue consists of gray matter, while the inner parts mainly consist of white matter. Furthermore, the brain is covered by meningeal layers, which separates the brain tissue from the cerebrospinal fluid (CSF). CSF fills up both the empty space between the brain and the skull, and the cavities within the brain, called the ventricles.

The fluid-filled spaces in between the cells in the tissue are referred to as the interstitial space. The brain tissue is also penetrated by numerous blood vessels, called the vasculature. The vasculature may act as sink for the therapeutic agent. However that is neglected in this study, and only spreading of the therapeutic agent in the interstitial space is considered. The effect of vascular uptake has been studied by, e.g., Smith and Humphrey (2007) and Baish et al. (1997).

The therapeutic agent can also undergo degradation and adsorption to the cells. These processes will obviously hinder the spreading of the drug. Morrison et al. (1994) included linear metabolism and adsorption. These processes were also included, among others, by Linninger et al. (2008b), but are not considered in this study, as we focus on the effects deformations, heterogeneities, and anisotropy have on the concentration distribution.

3 Model

3.1 Conceptual Model

A porous medium can be defined as a solid or a structure with interconnected voids, through which fluids can flow. Although the human body is a highly sophisticated system, the porous medium assumptions can be used to describe relevant features and processes in the interstitial space accurately (Nicholson 2001). Thus, one may consider the brain as a heterogeneous porous medium where the neurons and glial cells make up the solid phase filled by the interstitial fluid (Gillies et al. 2005). The interstitial space is highly tortuous and the pore sizes are of nanoscale. Nevertheless, it makes up 20% of the total volume of the brain (Nicholson 2001). Blood vessels, ventricle walls, and meningeal layers all contribute to the brain's heterogeneous structure. Moreover, different properties of the gray and white matters lead to both heterogeneity and anisotropy. Gray matter has a low permeability, but is relatively homogeneous and isotropic. On the other hand, white matter has a higher permeability, but is anisotropic. This anisotropy arises from the fibers formed by the axons in the white matter. Heterogeneities and anisotropy are important factors for transport processes in the tissue, and should be taken into account.

3.2 Mathematical Model

In this study, a poro-elastic model with patient-specific parameters and brain structure obtained from MRI is developed. The model is based on a 1D model developed by Gillies et al. (2005) and is here extended to 3D. Only the interstitial space and CED-induced transport processes are considered. For the mathematical model, the following assumptions were made:

- The therapeutic agent is completely soluble in the interstitial fluid.
- The fluid phase and the solid matter are both regarded as incompressible.
- The solid matrix is assumed to behave as an isotropic linear elastic material (small deformations).

- Changes in density and viscosity of the fluid phase as a result of dissolution of the therapeutic agent are neglected.
- The temperature is assumed to be constant.
- Chemical reactions, absorption, and adsorption of infused agents are neglected.
- Gravity force is neglected.

Thus, an equation for isothermal single-phase flow within an elastic matrix is solved for the fluid phase. To develop the flow equations, the solid matrix is taken into account as a second phase. The primary variables are the pressure (p) and the displacement ($\mathbf{u}$), and, in the transport equation, the molar concentration of therapeutic agent (c).

3.2.1 Flow Equations

Both fluid and solid phases are materially incompressible. However, the solid matrix is assumed to be deformable; i.e, the void space can change as a result of change in fluid pressure. Assuming the density of the solid and the liquid phase to be constant the mass balance can be transformed to a volume balance (see, e.g., Helmig 1997):

Solid phase:

$$\frac{\partial(1-\phi)}{\partial t} + \nabla \cdot ((1-\phi) \cdot \mathbf{v}_\mathrm{s}) = 0 \tag{1}$$

Fluid phase:

$$\frac{\partial \phi}{\partial t} + \nabla \cdot (\phi \mathbf{v}_\mathrm{l}) \pm \Omega_\mathrm{F}(\mathbf{x}, t) = 0 \tag{2}$$

Here $\mathbf{v}_\mathrm{s}$ and $\mathbf{v}_\mathrm{l}$ represent the velocities of the solid and fluid phases, respectively. ϕ is porosity and $\Omega_\mathrm{F}(\mathbf{x}, t)$ denotes source/sink terms of the fluid phase. Adding Eqs. 1 and 2 yields:

$$\nabla \cdot (\phi \mathbf{v}_\mathrm{l} + (1-\phi)\mathbf{v}_\mathrm{s}) \pm \Omega_\mathrm{F}(\mathbf{x}, t) = 0 \tag{3}$$

In the case of infinitesimal deformation, the velocity of the solid phase ($\mathbf{v}_\mathrm{s}$) can be represented by the partial time derivative of the displacement vector ($\mathbf{u}$):

$$\mathbf{v}_\mathrm{s} = \frac{D\mathbf{u}}{Dt} = \frac{\partial \mathbf{u}}{\partial t} \tag{4}$$

where $\frac{D}{Dt}$ denotes the material time derivative with respect to the solid phase velocity, which is approximated by the partial time derivative.

To describe the fluid flow in porous media on the continuum scale, generally the Darcy equation is applied. The Darcy equation represents a simplified momentum balance of the fluid phase (Hassanizadeh and Gray 1980). It is valid in the case of creeping flow (Reynolds number < 1) which can be assumed for brain tissue because of the small pores and flow velocities. Moreover, Reynolds number < 1 implies that inertial forces can be assumed negligible (Helmig 1997). For the poro-elastic case, there is an additional transport component since the displacement of the solid matrix contributes to movement of fluid within its pores. Thus, the transport velocity is:

$$\mathbf{v}_\mathrm{l} = -\frac{\mathbf{K}}{\phi \mu_\mathrm{w}} (\nabla p - \rho_\mathrm{l} \mathbf{g}) + \frac{\partial \mathbf{u}}{\partial t} \tag{5}$$

Here $\mathbf{K}$ represents the intrinsic permeability tensor, ρ_l is the fluid mass density, and μ_w is the viscosity of water which is assumed equal to the viscosity of interstitial fluid (ISF). Since

the fluid source is applied as a point source, the pressure gradient is steep and more important than gravity. Thus, gravity is assumed to be negligible. Substituting Eq. 5 in 3 and rearranging yields the final form of the fluid–solid mixture volume balance:

$$\nabla \cdot \left(\frac{\partial \mathbf{u}}{\partial t} - \frac{\mathbf{K}}{\mu_{\mathrm{w}}} \nabla p \right) = \Omega_{\mathrm{F}}(\mathbf{x}, t) \tag{6}$$

To set up a balance of forces in a porous medium, both the fluid and the solid phase have to be considered. As already mentioned, inertial forces and gravity are neglected. Thus, the only remaining forces are caused by the fluid pressure and by the stresses in the solid matrix.

$$\nabla \left(\sigma - p\mathbf{I} \right) = 0 \tag{7}$$

Further, the displacement vector ($\mathbf{u}$) can be related to the deformation or strain tensor field:

$$\mathbf{e} = \frac{1}{2} \left(\nabla \mathbf{u} + \nabla^{\mathrm{T}} \mathbf{u} \right) \tag{8}$$

Assuming an isotropic, linear elastic medium, it can be shown that the following linear stress–strain relation holds (Hassanizadeh and Gray 1980):

$$\sigma = 2\mu \mathbf{e} + \lambda (tr \mathbf{e}) \mathbf{I} \tag{9}$$

where μ and λ represent Lamé parameters. Substituting (9) and (8) into (7) and rearranging yields:

$$\nabla \cdot \left(\mu (\nabla \mathbf{u} + \nabla^{\mathrm{T}} \mathbf{u}) + \lambda (\nabla \cdot \mathbf{u}) \mathbf{I} \right) - \nabla p = 0 \tag{10}$$

Note that $\mathbf{u}$ and p are time-dependent due to Eq. 6. The Lamé parameters are used to characterize the elasticity of a medium and are related to the Poisson ratio (ν) and Young's Modulus (E) as follows:

$$\lambda = \frac{E\nu}{(1+\nu)(1-2\nu)}, \quad \mu = \frac{E}{2(1+\nu)} \tag{11}$$

For small values of μ and λ, deformation may occur even at low infusion pressure. While high values imply that the medium can be regarded as rigid.

3.2.2 Transport Equation

The transport equation can be derived from the mass balance of the infused therapeutic agent and results in the following equation:

$$\frac{\partial (c\phi)}{\partial t} + \nabla \cdot \left(\phi \mathbf{v}_{\mathrm{l}} c - \mathbf{D}_{\mathrm{pm}} \nabla c \right) = \Omega_{\mathrm{T}}(\mathbf{x}, t) \tag{12}$$

where c (mol/l^3) represents the concentration of the therapeutic agent and $\mathbf{D}_{\mathrm{pm}}$ is the effective diffusion tensor of the porous medium which in general is smaller than the diffusion coefficient of the agent in free water. $\Omega_{\mathrm{T}}(\mathbf{x}, t)$ (mol/sl^3) is a source/sink term for the therapeutic agent.

3.3 Effective Parameters

In an elastic medium, the structure of the solid phase is time-dependent. This should be taken into account in the model by relating medium properties to deformation.

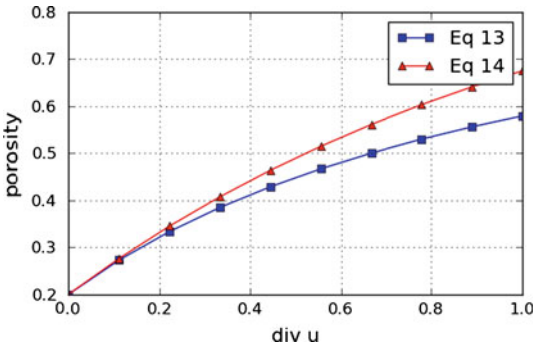

Fig. 1 The porosity is plotted versus displacement for an initial porosity of 0.2. For small deformations it can be seen that the different formulas do not make a difference, while for increasing divergence Eq. 14 results in lower porosity changes than the equation found in the literature

3.3.1 Porosity

Even though both fluid and solid phases are regarded as incompressible, their volume fractions can change due to local displacement. For small deformations the following relation between $\nabla \cdot \mathbf{u}$ and the porosity (ϕ) have been used (Netti et al. 1997):

$$\phi = \frac{\phi_0 + \nabla \cdot \mathbf{u}}{1 + \nabla \cdot \mathbf{u}} \tag{13}$$

This equation is employed in most poro-elastic models that include porosity changes (Gillies et al. 2005; Chen and Sarntinoranont 2007; Chen et al. 2002). However, an expression for the effective porosity can also be derived from the volume balance of the solid phase (Eq. 1) employing the approximation given in Eq. 4 for small deformation and the initial conditions $\phi = \phi_0$ and $\nabla \cdot \mathbf{u} = 0$. The result is:

$$\phi = 1 - (1 - \phi_0)e^{-\nabla \cdot \mathbf{u}} \tag{14}$$

In Fig. 1, porosity is plotted against the divergence of displacement for Eqs. 13 and 14. As long as the divergence of displacement ($\nabla \cdot \mathbf{u}$) is small the two formulas yield similar results. Small $\nabla \cdot \mathbf{u}$ is a result of gentle pressure gradients or high values of the Lamé parameters. When the divergence is large, the difference between Eqs. 13 and 14 increases. However, in the range were the linear elasticity theory holds, the two relations yield similar results and in this study Eq. 14 has been used.

3.3.2 Permeability

Zhang et al. (2000) showed that, during intra-tumoral infusion, an increase in the infusion pressure leads to significant changes in the permeability of the tissue. This is related to the deformation, which causes changes in size and connectivity between pores in the tissue. Tissue expansion may increase the conductivity and, thus, the permeability of the tissue in the vicinity of the injection point, whereas compression farther away closes the paths and may reduce permeability of the tissue (McGuire et al. 2006). Lai and Mow (1980) proposed the following exponential relationship between the deformation and the permeability:

$$\mathbf{K} = \mathbf{K}_0 e^{\beta \nabla \cdot \mathbf{u}} \tag{15}$$

Here $\mathbf{K}_0$ is the initial permeability tensor and β is a material constant. McGuire et al. (2006) fitted this parameter to results obtained from an experiment performed on both rodent and human tumor models. A sensitivity analysis was carried out and β was found to vary between

Table 1 Governing equations and boundary conditions

Volume balance	$\nabla \cdot \left(\frac{\partial \mathbf{u}}{\partial t} - \frac{\mathbf{K}}{\mu_w} \cdot \nabla p \right) = \Omega_F(\mathbf{x}, t)$
Displacement	$\nabla \cdot \left(\mu(\nabla \mathbf{u} + \nabla^T \mathbf{u}) + \lambda(\nabla \cdot \mathbf{u})\mathbf{I} - p\mathbf{I} \right) = 0$
Transport equation	$\frac{\partial (c\phi)}{\partial t} + \nabla \cdot \left(\left[c \left(-\frac{\mathbf{K}}{\mu_w} \cdot \nabla p + \phi \frac{\partial \mathbf{u}}{\partial t} \right) - \mathbf{D}_{pm} \nabla c \right] \right) = \Omega_T(\mathbf{x}, t)$
Porosity	$\phi = 1 - (1 - \phi_0) e^{-\nabla \cdot \mathbf{u}}$
Permeability	$\mathbf{K} = \mathbf{K}_0 e^{\beta \nabla \cdot \mathbf{u}}$
Diffusion	$\mathbf{J} = -\mathbf{D}_{pm} \nabla c$
Boundary conditions	$\mathbf{u} = 0$ cm on $\partial\Omega$
	$p = 400$ Pa on $\partial\Omega$
	$c = 0$ on $\partial\Omega$

0 and 5. Equation 15 was later employed in a poro-elastic model by Chen and Sarntinoranont (2007).

3.3.3 Diffusion

The last part of the second term in Eq. 12 represents diffusive flux. Diffusive flux is molecular transport caused by concentration gradients and can be described by Fick's 1st law (Nicholson 2001):

$$\mathbf{J} = -\mathbf{D}_{pm} \nabla c \quad \text{where } \mathbf{D}_{pm} = \phi \tau \mathbf{D}^* \tag{16}$$

$\mathbf{D}_{pm}$ is the effective diffusion tensor in a porous medium. $\mathbf{D}_{pm}$ is lower than the anisotropic aqueous diffusion tensor $\mathbf{D}^*$ obtained from diffusion tensor imaging, since the diffusion of therapeutic agent is limited to the porespace and since the connections between pores do not form straight channels. This is represented in Eq. 16 by the porosity (ϕ) and the tortuosity (τ). ϕ is time-dependent as given in Eq. 14, while τ is kept constant, a reasonable assumption for a convection dominated problem, since the diffusion is of less importance.The method of determination of the diffusion tensor ($\mathbf{D}^*$) and τ are explained in Sects. 4.2 and 4.2.3, respectively.

3.4 Numerical Implementation

The full set of governing equations are presented in Table 1. The equations are discretized and then implemented in a fully coupled flow and transport model based on a first-order Euler time discretization in combination with a BOX-discretization in space (Helmig 1997). The BOX-discretization is a vertex-centered finite volume scheme, which is constructed on a finite element mesh. It allows the application of unstructured grids by evaluating the gradients using finite element shape functions. The scheme is locally and, thus, globally mass conservative, since the BOX-discretization is based on finite volumes. The discretized equations were then implemented in the $DuMu^x$ framework (Flemisch et al. 2011).

4 Determination of Parameters

To apply the model described above to realistic cases, information about the properties of the tissue is needed. Since every human is unique, patient-specific parameters must be found

in vivo. In this article, information from magnetic resonance imaging (MRI) of a patient is interpreted to determine effective model parameters. From diffusion tensor imaging (DTI), we use the self-diffusion tensor of water in brain tissue ($\mathbf{D}_{s-d}$) to characterize the degree of heterogeneity and anisotropy. Furthermore, information from the DTI data are used to delineate geometrical boundaries. For an overview of diffusion-weighted MRI, we refer to Hagmann et al. (2006).

4.1 Parameters from Literature

In the future, all patient-specific parameters should be obtained non-invasively. Currently, literature values are needed for initial porosity (ϕ_0), the Lamé parameters (μ and λ), and for the calibration of K and D described below. Bender and Klose (2009) proposed a method for determining porosity from MRI that showed promising results. For the elasticity parameters, more research is still needed, but we believe that elastography will be a useful tool in the future (see, e.g., Klatt et al. 2007 or Cheng et al. 2008). However, in the scope of this study, the parameters are based on average values found in the literature (see Smith and Humphrey 2007 for a review). In general, these values have been measured using animal models, and are not human brain data.

4.2 Diffusion Tensor Imaging (DTI)

In this study, diffusion tensor images (DTI) are obtained from a patient at OVGU-Magdeburg University Hospital, Germany. Each 3D image represents one of the components of the self-diffusion tensor of water in the brain tissue ($\mathbf{D}_{s-d}$) and consists of $128 \cdot 128 \cdot 65$ voxels with a resolution of 2 mm. All calculations performed in the following are based on this data-set.

Basser et al. (1994b) showed how $\mathbf{D}_{s-d}$ in human tissues can be estimated from spin-echo experiments using multiple regressions. Later, Basser et al. (1994a) also verified how this technique can be used to determine the orientation of white matter fiber tracts; the eigenvector corresponding to the largest eigenvalue of $\mathbf{D}_{s-d}$ defines the tissue's fiber tracts axis (z-axis), while the two remaining perpendicular eigenvectors define the x- and y-axes. Then, after preprocessing the raw data, $\mathbf{D}_{s-d}$ can be represented voxel wise as a positive definite symmetric tensor.

A general macroscale transport tensor, e.g., electrical conductivity or diffusion tensor, can be related to the microstructures of the medium through its statistical moments (Brown 1955; Sen and Torquato 1988). Tuch et al. (2001) demonstrated how this principle can be used to link $\mathbf{D}_{s-d}$ to the electrical conductivity of biological tissue. Further, they proposed that the same principle can be used to estimate the diffusion of macromolecules ($\mathbf{D}^*$) within the tissue and the permeability ($\mathbf{K}_0$) of the tissue.

The mathematical model used in this study assumes anisotropic permeability and diffusion tensors, whereas the elastic properties are assumed to be isotropic. Even though the fiber structure of the white matter suggests anisotropic elastic properties, this issue is still under debate (Cheng et al. 2008). Odgaard et al. (1997) and Odgaard (1997) showed that mechanical anisotropy directions are aligned with the directions of the fiber structure in cancellous bone. More recently, Cowin and Cardoso (2011) developed a poro-elastic model that takes anisotropic elasticity into account, with application to cancellous bone. However, it is still an open question whether the elastic properties of brain tissue align with the fiber tracts (Cheng et al. 2008). Therefore, we have chosen to model the brain tissue as an isotropic elastic material.

Sarntinoranont et al. (2006) calculated **K** and **D*** tensors for the spinal cord of a rat and Linninger et al. (2008a) obtained the same parameters for a human brain. The main assumption behind this principle is, as Basser et al. (1994b) and Tuch et al. (2001) proposed, that $\mathbf{D}_{s-d}$, **K** and **D*** share the same set of eigenvectors. In the article by Sarntinoranont et al. (2006), the eigenvalues in the white matter regions are assumed to be equal in x- and y- directions, while a significantly higher value is assumed in the z-direction. This is a reasonable assumption for the spinal cord, where the orientation of most of the fiber tracts is in the z-direction. In the brain tissue, the orientation of the fiber tracts is heavily dependent on the location. But the eigenvalues can be calibrated to the eigenvalues of the self-diffusion tensor following a three-step calibration procedure proposed by Linninger et al. (2008a). Below we describe the calibration of the initial permeability field ($\mathbf{K}_0$); exactly the same principle is used to obtain **D***.

4.2.1 Initial Permeability, $\mathbf{K}_0$

In the first step, the diffusion tensor ($\mathbf{D}_{s-d}$), obtained from DTI, is decomposed into eigenvectors (ξ) and eigenvalues (λ_{i_w}) for each voxel:

$$\mathbf{D}_{s-d} = \xi \cdot \mathbf{\Lambda} \cdot \xi^{\mathrm{T}} \quad \text{where } \mathbf{\Lambda} = \begin{bmatrix} \lambda_{1_w} & 0 & 0 \\ 0 & \lambda_{2_w} & 0 \\ 0 & 0 & \lambda_{3_w} \end{bmatrix}. \tag{17}$$

In the second step, the mean of the eigenvalues ($\bar{\lambda}_w$) is found and then the eigenvalues are scaled by $\bar{\lambda}_w$. The result is multiplied by a typical value of the permeability (K) obtained from the literature, to obtain eigenvalues of the initial permeability field:

$$\bar{\lambda}_w = \frac{1}{3}\Sigma_{i=1}^{3}\lambda_{i_w} \quad \text{and} \quad \lambda_{i_K} = K\left(\frac{\lambda_{i_w}}{\bar{\lambda}_w}\right) \tag{18}$$

Finally, in step 3 the initial permeability tensor ($\mathbf{K}_0$) is calculated:

$$\mathbf{K}_0 = \xi \cdot \mathbf{\Lambda}_{\mathbf{K}} \cdot \xi^{\mathrm{T}} \quad \text{where } \mathbf{\Lambda}_{\boldsymbol{K}} = \begin{bmatrix} \lambda_{1_K} & 0 & 0 \\ 0 & \lambda_{2_K} & 0 \\ 0 & 0 & \lambda_{3_K} \end{bmatrix}. \tag{19}$$

As mentioned above, the initial permeability tensor is assumed to have the same eigenvectors as the diffusion tensor. In Fig. 2, results of the calibration for $\mathbf{K}_0/K$ are presented to show the anisotropy of the brain tissue.

The method proposed by Linninger et al. (2008a) requires a reference value for the permeability (K). Based on pressure fields measured during CED in clinical trials (Bobo et al. 1994; Prabhu et al. 1998), an average permeability value of $K = 1.82 \times 10^{-15}\,\mathrm{m}^2$ was calculated by Smith and Humphrey (2007). In this study, $K = 1.82 \times 10^{-15}\,\mathrm{m}^2$ is applied unless otherwise is stated. However, a wide range of permeability values can be found in the literature; see, e.g., Basser (1992) and Kaczmarek et al. (1997). Moreover, the permeability in white matter is often assumed to be significantly higher than in gray matter (see Sect. 5).

4.2.2 Diffusion Tensor, $\mathbf{D}^*$

The diffusion tensor ($\mathbf{D}^*$) is obtained in the same manner as the effective permeability ($\mathbf{K}_0$). The only difference is that now the calibration of the eigenvalues is given as:

$$\lambda_{i_D} = D\left(\frac{\lambda_{i_w}}{\bar{\lambda}_w}\right) \tag{20}$$

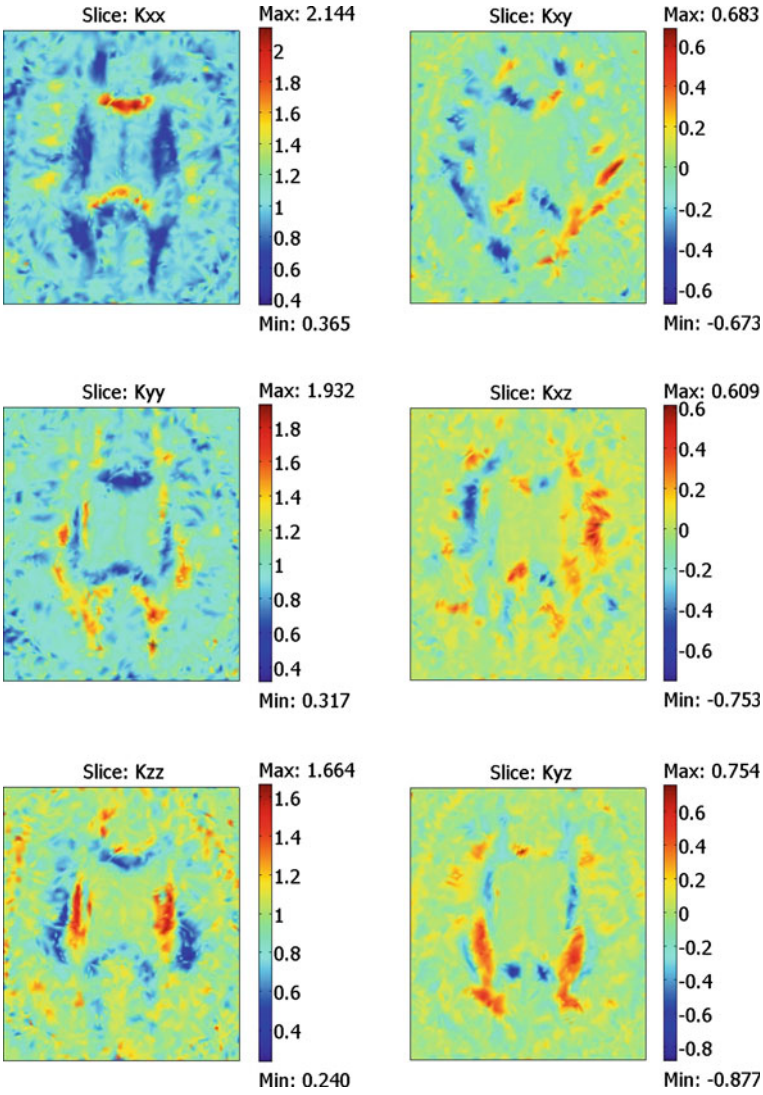

Fig. 2 A cross section of the six components of the DTI-dataset after performing the calibration proposed by Linninger et al. (2008a). Note that the plots represents $\mathbf{K}_0/K$ and, thus, the anisotropic features of the tissue. The *left column* shows the components of the main diagonal of the normalized tensor, while the *right* represents the off-diagonals of the symmetric tensor. In the most anisotropic regions $K_{xx} \approx 7K_{yy}$

Note that D is the free diffusion coefficient of the contrast agent Gd-DTPA in water, which is equal to $D = 3.8 \times 10^{-10}\,\mathrm{m}^2/\mathrm{s}$ (Kim et al. 2005). Finally, $\mathbf{D}^*$ becomes:

$$\mathbf{D}^* = \xi \cdot \mathbf{\Lambda_D} \cdot \xi^{\mathrm{T}} \quad \text{where } \mathbf{\Lambda_D} = \begin{bmatrix} \lambda_{1_D} & 0 & 0 \\ 0 & \lambda_{2_D} & 0 \\ 0 & 0 & \lambda_{3_D} \end{bmatrix}. \tag{21}$$

4.2.3 Tortuosity (τ)

The calibration of $\mathbf{D}^*$ takes the anisotropy into account, but not the tortuosity (τ). τ is calculated from DTI-data defining tortuosity as the square root of effective diffusion measured in DTI (Vorisek and Sykova 2009) divided by the free self-diffusion coefficient of water (D_w). D_w is here taken to be $3.22 \times 10^{-9}\,\mathrm{m}^2/\mathrm{s}$ which holds for water at 40°C (Holz et al. 2000). The tortuosity is kept constant and its value is based on the trace of $\mathbf{D}_{s-d}$ in the DTI-data

$$\tau = \sqrt{\frac{\frac{1}{3}\left(D_{xx} + D_{yy} + D_{zz}\right)}{D_\mathrm{w}}} \tag{22}$$

The diffusion of water in the tissue cannot exclusively be assigned to the extracellular space. Since water can diffuse through the cells, the diffusion tensor obtained from DTI overestimates the tortuosity of the medium (Vorisek and Sykova 2009).

4.3 Geometry

From MRI, the anatomy of the brain can be reconstructed. Obviously, this is important since different brain structures have different transport properties. This reconstruction should delineate white matter and gray matter regions, ventricles and meningeal layers. All these structures play an important role when modeling the flow and transport processes in the brain. Reconstruction can be done applying algorithms such as noise filtering, contrast enhancement, and edge detection to MR-images. From this, a domain corresponding to the shape of the brain is created. These are rather time-consuming methods. Therefore, in this study a voxel-based approach was used. This was also done in a study by Kim et al. (2009, 2010). In this approach, a dimensionless index, called fractional anisotropy (FA), is used to distinguish between white and gray matters. FA is calculated based on the eigenvalues obtained from DT-images:

$$\mathrm{FA} = \sqrt{\frac{3}{2} \cdot \frac{\left(\lambda_{1_w} - \bar{\lambda}\right)^2 + \left(\lambda_{2_w} - \bar{\lambda}\right)^2 + \left(\lambda_{3_w} - \bar{\lambda}\right)^2}{\lambda_{1_w}^2 + \lambda_{2_w}^2 + \lambda_{3_w}^2}} \tag{23}$$

where $\bar{\lambda}$ is the mean of the eigenvalues defined in Eq. 18. This index was proposed by Basser and Pierpaoli (1996) and is a measure of the fraction of $\mathbf{D}_{s-d}$ which can be assigned to anisotropic diffusion. For an isotropic medium, FA is 0, while for an axisymmetric anisotropic medium FA = 1. Since brain tissue is neither axisymmetric nor isotropic, the FA values lie somewhere between 0 and 1. In this study, voxels with FA > 0.4 are defined as white matter (Table 2). This is done based on the FA values shown in Fig. 3. Distinguishing between gray matter and white matter is important since the infused agents spread over larger volumes in white than in gray matter. For low-resolution MR-images, the probability that the signal from one voxel only represents one tissue type is pretty low. This leads to another uncertainty in this parameter. But, in the future, higher resolution images will solve this problem.

Table 2 Based on threshold values, it is distinguished between different regions and tissue types in the brain

	FA	τ
Gray matter	0–0.4	0.24–0.54
White matter	>0.4	0.24–0.54
Ventricle/meninges	–	<0.24 or >0.54

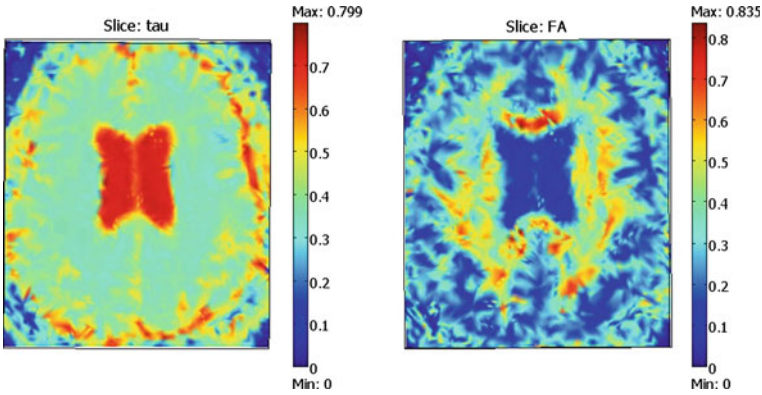

Fig. 3 Cross section of the tortuosity calculated using Eq. 22 (*left*). Fractional anisotropy (FA) calculated using Eq. 23 (*right*)

To delineate ventricles, meningeal layers, and bones from the parenchyma, the tortuosity field (see Sect. 4.2.2) is used. The threshold values applied are given in Table 2. This approach works well for the ventricles, but again the resolution is too low to successfully delineate the meningeal layers.

5 Results and Discussion

5.1 Simulations for the Homogenous and Isotropic Case

To test the capability of the model, 3D simulations were performed on a homogenous and isotropic domain. Dirichlet boundary conditions were imposed, i.e., displacement ($\mathbf{u}$) and concentration (c) were set to zero and pressure (p) to 400 Pa at the outer boundaries. The modeled domain was $4 \cdot 4 \cdot 4\,\mathrm{cm}^3$ and the gridspacing was 2 mm using a regular cubic grid. The simulations were performed for 2 h with an initial timestep size of 5 s. A source term representing a constant infusion rate of 0.3 ml/h (5 µl/min) was assigned to one node in the center of the domain. This fills up one finite volume box, which can be interpreted as a catheter with a diameter equal to the grid spacing. Similar infusion rates were used in the models by Linninger et al. (2008b) (4 µl/min) and Smith and Garcia (2011) (6 µl/min). The concentration of the therapeutic agent in the infused fluid was set to 10^{-7} mole of Gd-DTPA per mole water. The pressure was time-dependent (see Eq. 6), but after approximately 1 h it reached steady state. Due to mixing of the infused fluid and the ISF it took a few minutes before the concentration in the interstitial space equaled the concentration in the infused fluid.

The current model was compared to the linear elastic model by Chen and Sarntinoranont (2007) and the hyperelastic model by Smith and Garcia (2011), with the same parameter values as they used in their studies. The current model yields similar results for pressure and deformation as the model by Chen and Sarntinoranont (2007), but due to different boundary conditions (assignment of source), the concentration distribution is different. Compared to the model by Smith and Garcia (2011) the concentration distribution in the interstitial space is similar, but the displacement and pressures are different, since they used a non-linear elastic model.

Table 3 Literature values used in the simulations (Smith and Humphrey 2007; Kim et al. 2005; Nicholson 2001; McGuire et al. 2006; Chen and Sarntinoranont 2007)

Parameter	Symbol	Value	Unit
Permeability	K_0	1.82×10^{-15}	m^2
Viscosity of water	μ_w	9.11×10^{-4}	Pa s
Molar density of water	ρ_{mol}	55500	mol/m^3
Diffusion coefficient Gd-DTPA	D	3.8×10^{-10}	m^2/s
Porosity	ϕ_0	0.2	–
Tortuosity	τ	0.4	–
Young's Modulus	E	5000	Pa
Poisson ratio	ν	0.4	–
Material constant	β	2	–

In the following, a grid convergence test is presented. Then, the initial permeability, Young's modulus and Poisson ratio are varied, this can give an indication of sensitivity in our results to the range of realistic parameter values (Sect. 5.1.2). Finally, the poro-elastic model used in this study is compared to the rigid assumption case, to see whether including elasticity yields significantly different results (Sect. 5.1.3).

5.1.1 Grid Convergence

To check whether the mesh is sufficiently refined a grid convergence test was performed with three different gridspacings; 2, 2/3, and 2/9 mm. The parameters given in Table 3 were used and the source term was assigned to a volume of 8 mm^3 for all cases. The results can be seen in Fig. 4. Since the source term was distributed over more nodes when the mesh was refined, a significantly lower peak pressure in the middle can be seen. However, the peak pressure values converged with increasing grid resolution, as can be seen in Fig. 4. With respect to the displacement, the maximum values are highest for the lowest resolution. For the two cases with the finer meshes, the displacement becomes more distributed and converges to the same result. Nevertheless, the concentration distribution, which was of major interest in this study, was similar for all cases.In all the following simulations the gridspacing was 2 mm and one should have this in mind interpreting the results.

5.1.2 Choice of K Values and Elastic Properties

Even though permeability values for brain tissue can be found in the literature, there is still a large uncertainty in this parameter. In clinical trials, significantly less spreading of the infused agent has been observed in gray matter than in white matter (Bobo et al. 1994; Prabhu et al. 1998). To take this into account, Kaczmarek et al. (1997) assumed the permeability of white matter to be 100 times larger than that of gray matter. Based on this, both Linninger et al. (2008a) and Sarntinoranont et al. (2003, 2006) used $K_{wm} = 100K_{gm}$ in their studies.

We performed simulations for three different K values, $K = 1.82 \times 10^{-15}\,m^2$, $1.3 \times 10^{-16}\,m^2$, and $1.3 \times 10^{-14}\,m^2$ and the effects on the pressure field, the porosity field and the concentration distribution was investigated. Note that according to Eq. 6 the permeability was divided by the viscosity. The results can be seen in Fig. 5 where the three different permeability values are compared. The time to steady state is significantly larger for low

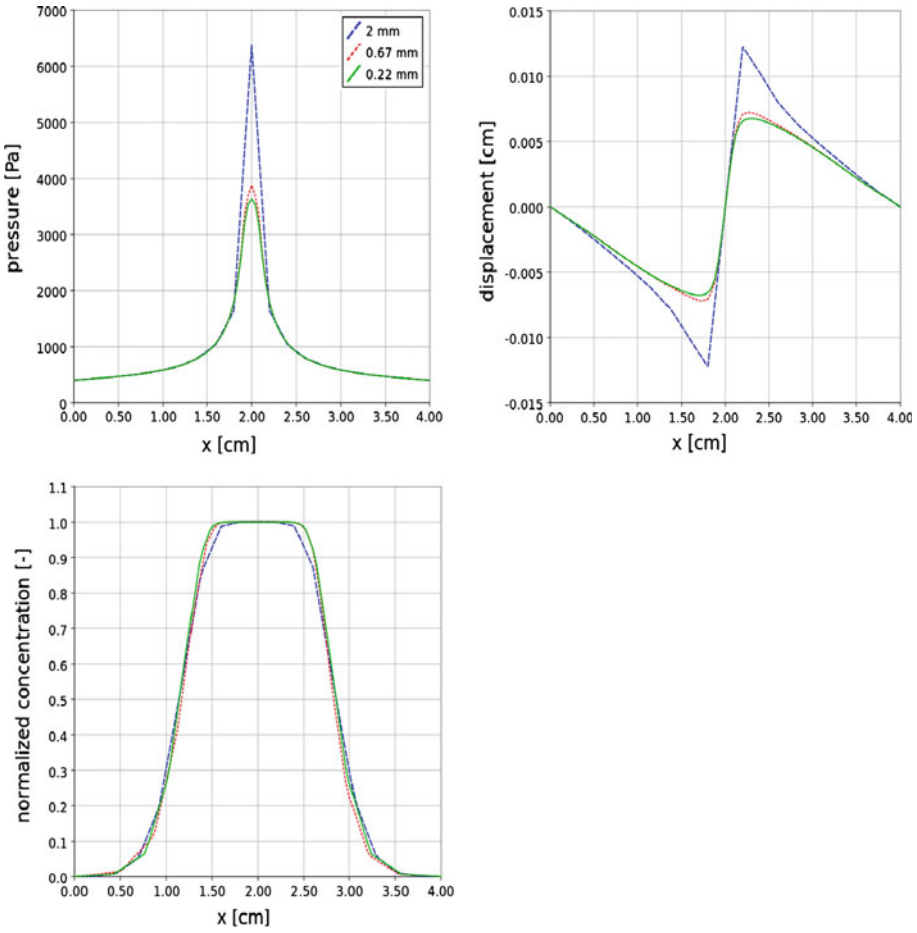

Fig. 4 Results from the grid convergence simulations

permeability values than for high values, since low permeability leads to steeper pressure gradient, higher deformation and a longer consolidation period. However, after 2 h, steady state is reached even for the low permeability case.

As already mentioned, the value found by Smith and Humphrey (2007) was used as the reference value for the permeability. This value is based on measured pressure increases, relative to the intracranial pressure, during CED into white matter of a cat brain (Bobo et al. 1994) and into gray matter of a rat brain (Prabhu et al. 1998). In the study by Bobo et al. (1994), the observed pressure increase is approximately 2.4 kPa for an infusion rate of 0.07 ml/h. Employing permeability values of 1.82×10^{-15} m^2, yields maximum pressures that agree with this; an infusion rate of 0.1 ml/h resulted in a pressure increase of 2.6 kPa (results not shown). The two other permeability values employed, 1.3×10^{-16} m^2 and 1.3×10^{-14} m^2, are also within the range of the values employed in other numerical models (see Sect. 4.2). However, the lowest permeability value leads to a pressure increase of about 30 kPa in the infusion center. On the other hand, the highest permeability causes a pressure increase of only about 1 kPa. Therefore, with the current Young's moduli values the permeability value

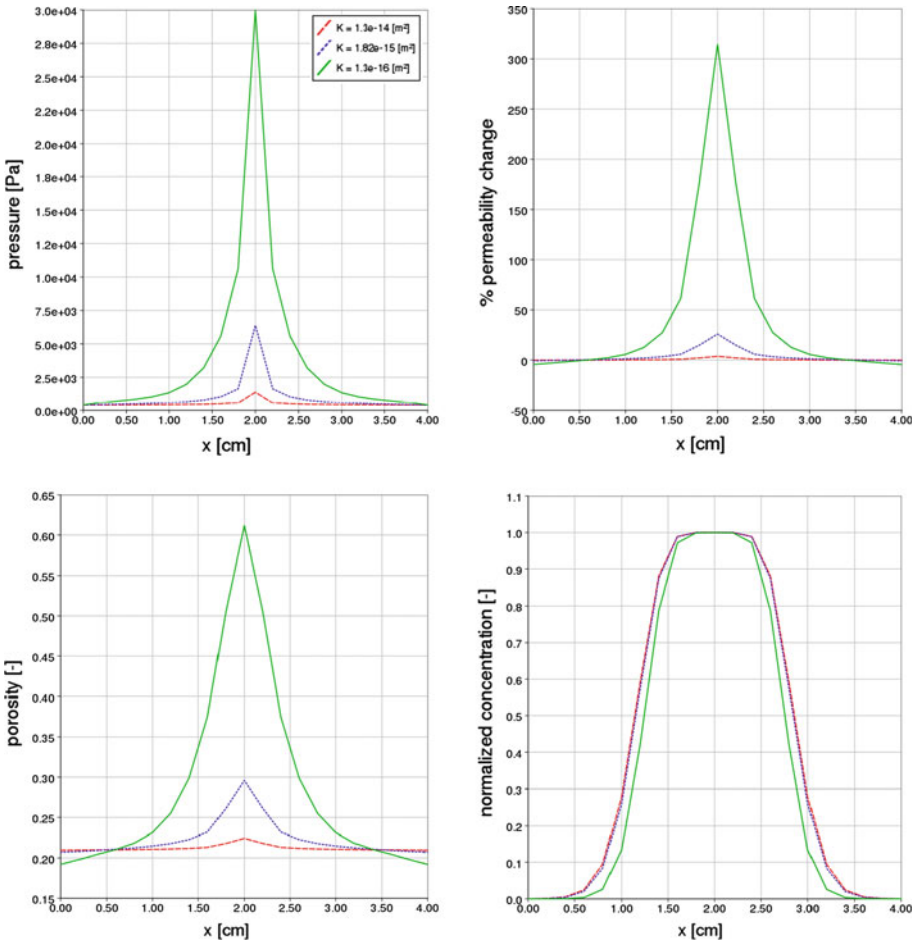

Fig. 5 Results from simulations with different K values

calculated by Smith and Humphrey (2007) seems most realistic. However, since the brain tissue is heterogeneous, we can expect similar pressure increases in regions with low permeability if the low permeability zone is small. Similarly, high pressure increases can occur in high permeability regions if the surroundings have a significantly lower permeability. Thus, a homogeneous and isotropic model domain is inadequate to describe the pressure fields observed in clinical trials.

In this study, linear elasticity is assumed and elastic parameters based on Smith and Humphrey (2007) and Chen and Sarntinoranont (2007) are used. However, in recent nonlinear elastic models (Dutta-Roy et al. 2008; Smith and Garcia 2009, 2011) significantly lower Young's moduli (E) based on a study by Miller and Chinzei (2002) have been used. To see how this affects the results, simulations were conducted with $E = 421$ (Miller and Chinzei 2002) and $\nu = 0.35$. In Fig. 6, the results from using both set of parameters are compared. The pressure values are significantly lower using the values from Miller and Chinzei (2002) than the ones from Smith and Humphrey (2007). This is because the displacement are larger, which according to Eqs. 14 and 15 lead to increased porosity and permeability changes,

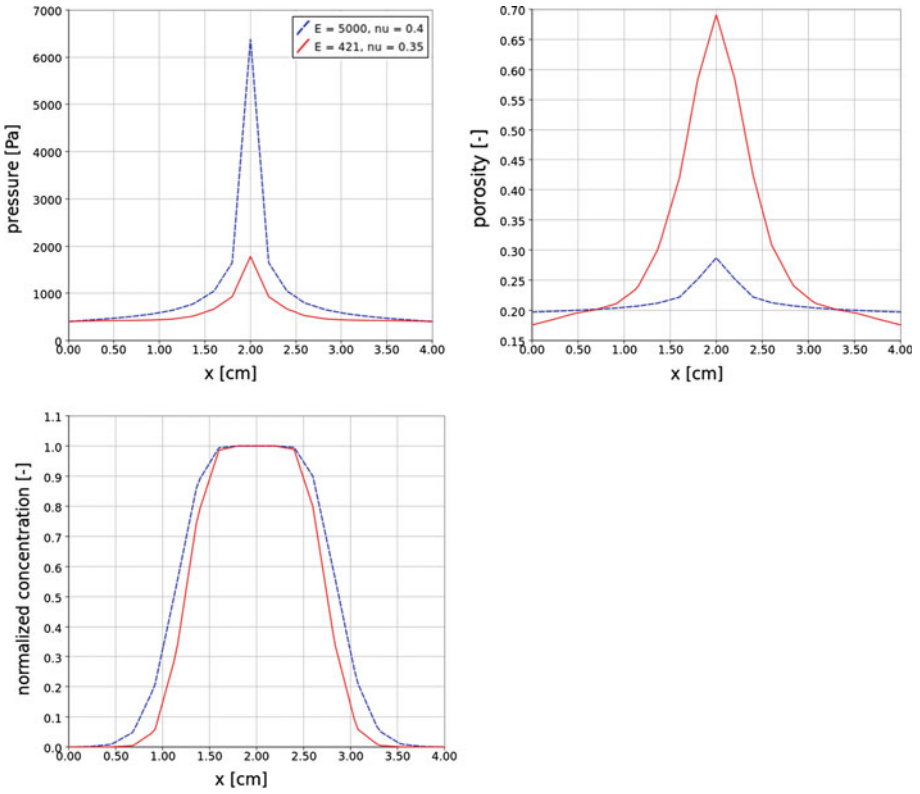

Fig. 6 Comparison of the Young's modulus (E) and Poisson ratio (ν) used in this study and the values from Miller and Chinzei (2002)

respectively. Note that $E = 421\,\text{Pa}$ results in such large porosity changes that the choice of relation between displacement and porosity becomes more important (see Eq. 14). Finally, the drug spreads to a smaller extent due to larger storage as a result of the increased porosity. Additionally, the porosity and permeability decrease farther away from the infusion site and hinders flow.

5.1.3 Rigid Versus Elastic model

As discussed in Sect. 1.1.1, often the assumption has been employed that in models describing flow and transport during CED, brain tissue deformation is negligible. To test this assumption, the result from the elastic model were compared to the from a rigid model using the same parameters, grid spacing, and domain size, as in the previous section. Again, the simulations were performed for 2 h and the results can be seen in Fig. 7. Comparing the results of the rigid and the elastic model for $K = 1.82 \times 10^{-15}\,\text{m}^2$ a difference in pressures is observed; this is due to changes in the permeability. However, with a Young's modulus of 5000 Pa, there is no significant difference between the resulting concentration distributions. Only for the lowest permeability value, $K = 1.3 \times 10^{-16}\,\text{m}^2$, a difference in the distribution could be seen, but this created unreasliticly high pressure increases. In Fig. 7, the pressure and concentration distribution after 15 min and 2 h are shown for $K = 1.3 \times 10^{-16}\,\text{m}^2$. Due to permeability

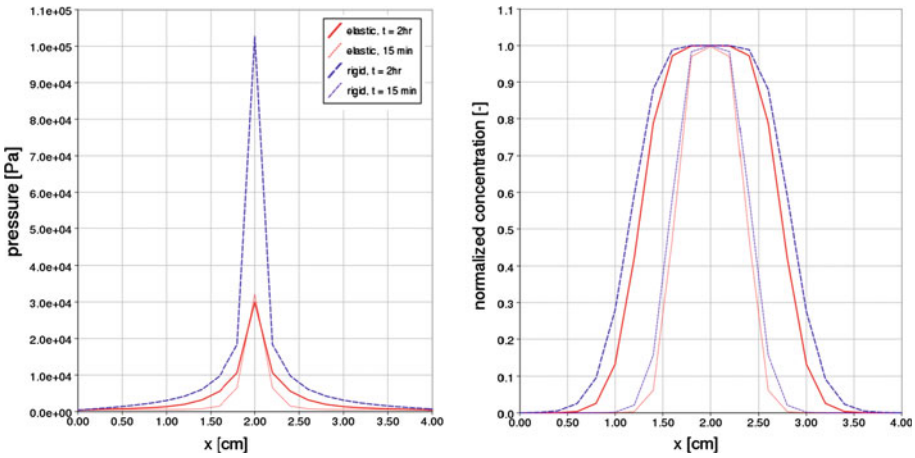

Fig. 7 Comparison of pressure and concentration distribution for a rigid and an elastic model. In the elastic model lower pressure increases and less spreading of the therapeutic agent are observed

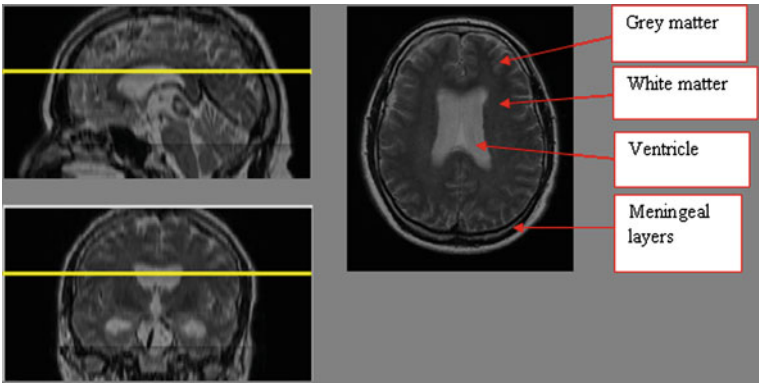

Fig. 8 T_2 weighted MR-image of the same patient as the DT-images described in Sect. 4.2. The cross section that can be seen to the right is through the line that can be seen from the left image. The different compartments are shown. Note that white matter appears darker than gray matter

changes, the elastic model produces a significantly lower pressure than the rigid model and, as expected, less spreading of the therapeutic agent is observed. Note that using the Young's modulus from Miller and Chinzei (2002), the difference would be significant also for the permeability value of 1.82×10^{-15} m^2 (see Fig. 6). Therefore, we conclude that it is important to take deformations into account in numerical models describing CED.

5.2 Implementation of Patient-Specific Parameters and Brain Structure

One of the main aims of this study is to investigate effects of anisotropy and heterogeneities on the final concentration distribution of therapeutic agents in brain tissue. As explained in Sect. 4.3, FA was used to distinguish between gray and white matters and the tortuosity was used to delineate the ventricles, meningeal layers, and bones from the brain tissue (see Fig. 8). Since the resolution of the DTI is quite low and only the transport within the

parenchyma was considered, the meningeal layer, ventricles, and bones were lumped together. Thus, we only distinguished between inside and outside the brain tissue and a low permeability was assigned to elements outside the parenchyma to mimic a no-flow boundary condition. The calibrated diffusion tensor and permeability tensors were used to account for heterogeneities and anisotropy of the tissue. These parameters were all read from a file and assigned element wise, where the voxel size in the DT-images equaled the size of the grid cells, i.e., $2 \times 2 \times 2\,\text{mm}^3$. The parameter values taken from the literature were the same as given in Table 3, unless otherwise specified. Due to computational limits, simulation of the whole brain was not possible; instead a smaller volume of interest (VOI) were studied. All simulations were performed for 12 h with an infusion rate of 0.3 ml/h, and the infusion concentration was, as in the previous section, set to 10^{-7} mole of Gd-DTPA per mole water. In the plots, the normalized concentration is displayed; i.e., the actual concentration divided by the concentration of the agent in the infused fluid.

As in Sect. 5.1, we employ Dirichlet boundary conditions (see Table 1). Which means that the displacement is forced to zero at the boundary of the VOI. Moreover, we cannot run long simulations since the drug will reach the boundary of the domain after a certain period of time.

The permeability value needed in the calibration procedure of Linninger et al. (2008a) for white matter was set to $1.82 \times 10^{-15}\,\text{m}^2$ (Smith and Humphrey 2007). To capture the resistance to the flow in gray matter regions, a reference K of one order of magnitude lower was assigned to it. Finally, outside the brain tissue, a K value of three orders of magnitude lower than for gray matter was assigned. Darcy's law is not applicable for these regions since they represent free flow regions. However, since the meningeal layers and the boundaries to the ventricles are not resolved and it is assumed that the therapeutic agent cannot freely pass these boundaries, a low permeability was assigned to the entire region and Darcy's law was applied. For the porosity, it was also distinguished between gray and white matter and inside and outside the brain tissue.

5.2.1 Spreading in 3D

A VOI was chosen as shown in Fig. 9 (1). The size of the domain was $6.0 \times 9.6 \times 5.4\,\text{cm}^3$, with 38 840 nodes. The results can be seen in Fig. 9. Note that the porosity field is shown in the background and that white matter appears black since it has lowest porosity. The isolines show the pressure field, divergence of the displacement, and the normalized concentration distribution, in Fig. 9 (2), (3), and (4), respectively. The divergence of the displacement is shown since both the porosity changes and the permeability changes will follow the same distribution pattern. Comparing the results with the isotropic case, the magnitudes of the primary variables are similar, but the distributions are significantly different. The results clearly show preferential flow in the white matter regions and it follows the pattern of the fiber tracts (see Sect. 4.2). Moreover, the location of the infusion is chosen in a region where the diffusion component in z-direction is large. This can clearly be seen as the agent spreads most in z-direction.

5.2.2 Effect of Different Permeability Fields

For the simulations described here, a different VOI was chosen to investigate how the location of the infusion affects the concentration distribution. This VOI represented the whole cross section in the xy-plane and 1.6 cm in z-direction, which translates to a domain of

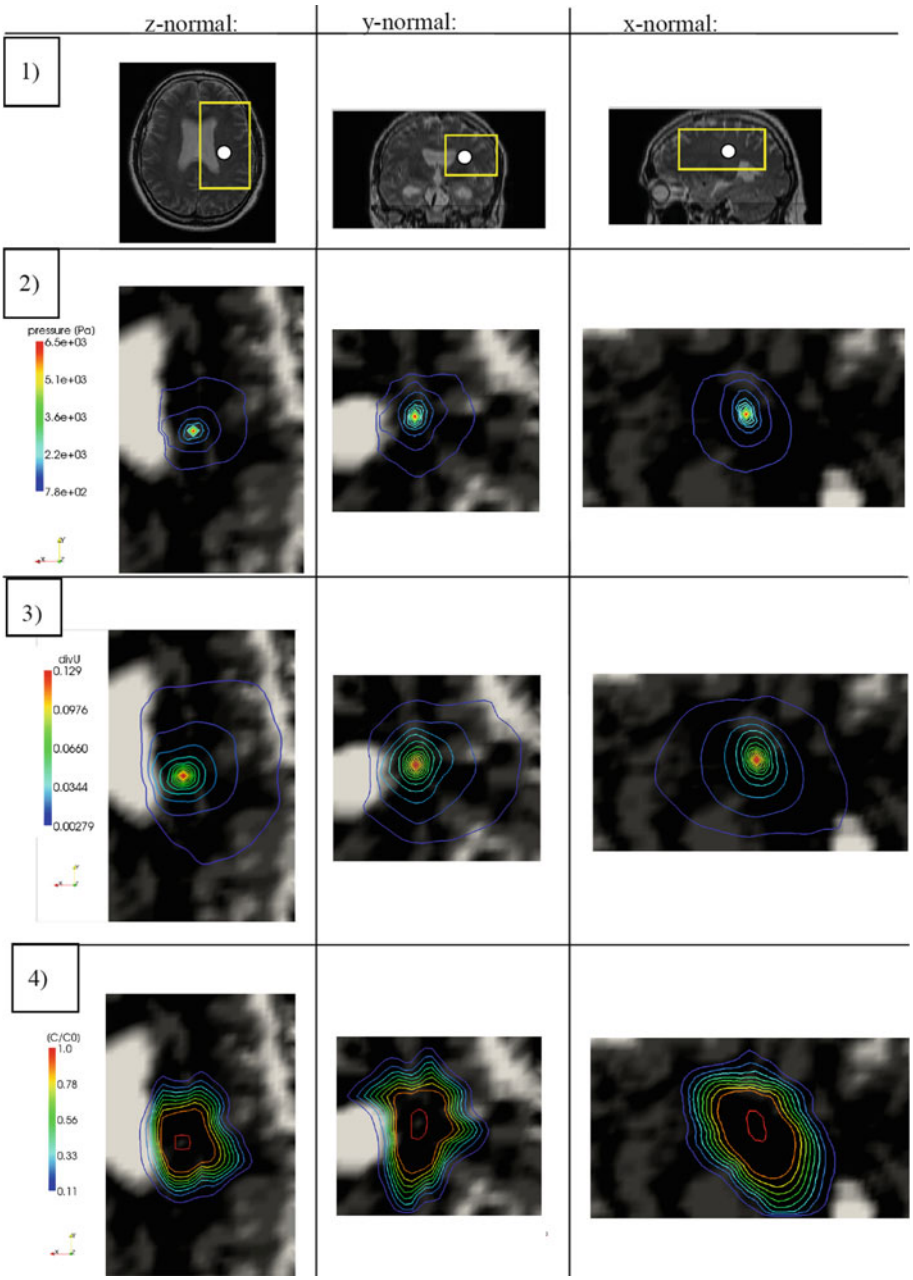

Fig. 9 Plots showing the results after 12 h of infusion at a rate of 3 ml/h based on the the DTI data set from OVGU-Magdeburg University Hospital. (*1*) Cross sections showing the modelled domain. (*2*) Pressure fields. (*3*) Divergence of the displacement, which is shown since both the porosity changes and the permeability changes will follow the same distribution pattern. (*4*) Concentration distribution. Note, that agent spreads most in z-direction

Table 4 Different permeability values (m^2) assigned to the different regions

	Calibration	Outside	Gray matter	White matter
Case 1	No	1.3×10^{-19}	1.82×10^{-15}	1.82×10^{-15}
Case 2	Yes	1.3×10^{-19}	1.82×10^{-15}	1.82×10^{-15}
Case 3	Yes	1.3×10^{-19}	1.3×10^{-16}	1.82×10^{-15}
Case 4	Yes	1.3×10^{-13}	1.3×10^{-16}	1.82×10^{-15}

$14 \times 16.2 \times 1.6\,\text{cm}^3$ with 45 360 nodes. In the following, four different cases with different permeability fields (given in Table 4) are compared. The source term, i.e., the location of the infusion, was set at three different locations in the xy-plane (see Fig. 10). In Case 1, all parameters were initially kept constant, apart from a lower permeability value assigned to the regions defined to be outside the brain tissue. As no calibration of the permeability and diffusion coefficient was done, the brain tissue was assumed to be homogeneous and isotropic. In Case 2, the calibration was performed, but K was set to be equal for gray and white matters. In the two latter cases $K_{\text{wm}} = 10K_{\text{gm}}$. Thus, Case 3 was identical with the simulation done in the previous section, while in Case 4 the permeability outside the brain tissue was set to be three orders of magnitude higher than for the gray matter.

As can be seen in Fig. 10, the results of Case 1 show that the agent spreads spherically from the injection point apart from in the vicinity of the ventricles. For Case 2, the effect of the anisotropy and heterogeneities as a result of the calibration procedure can be seen. However, in Case 3, the preferential patterns are more evident since K of white matter is one order of magnitude higher than that of gray matter. If results from clinical trials, which indicate similar permeability for gray and white matters, are valid, then the question arises whether Case 2 is sufficient to describe the flow pattern seen during CED. The reason for the resistance to the flow in gray matter is still an open question, but may be related to difference in elastic properties of the media. It could be that there are stronger permeability changes in gray matter than in white matter. If gray matter has a significantly lower Young's modulus than white matter lower pressures and less spreading could be explained by larger deformations in gray matter. Another explanation could be that the coefficient β needed in non-linear equation for the permeability change (Eq. 15) is significantly different for gray and white matters. Implementing this, the model may reproduce similar pressure elevation in both regions, even though the permeability and Lamé parameters are in the same order of magnitude. But, this does not explain the physical reason for the observed flow resistance.

In Case 4, the assumption that macromolecules are hindered from entering the CSF was tested. If macromolecules are free to pass the meningeal layers a much larger leakage to CSF will be observed. This is done by assigning a high permeability to the regions defined outside the brain and shows a significant leakage to CSF if the injection was done in the vicinity of the ventricles.

6 Summary and Conclusion

The purpose of this study is to show the workflow from MRI measurements to a computational model with realistic parameters. Patient-specific anatomy and parameters were implemented in a numerical model, which describes flow and transport in an elastic deformable matrix. Information about the anatomy, heterogeneities, and anisotropy of the tissue was obtained

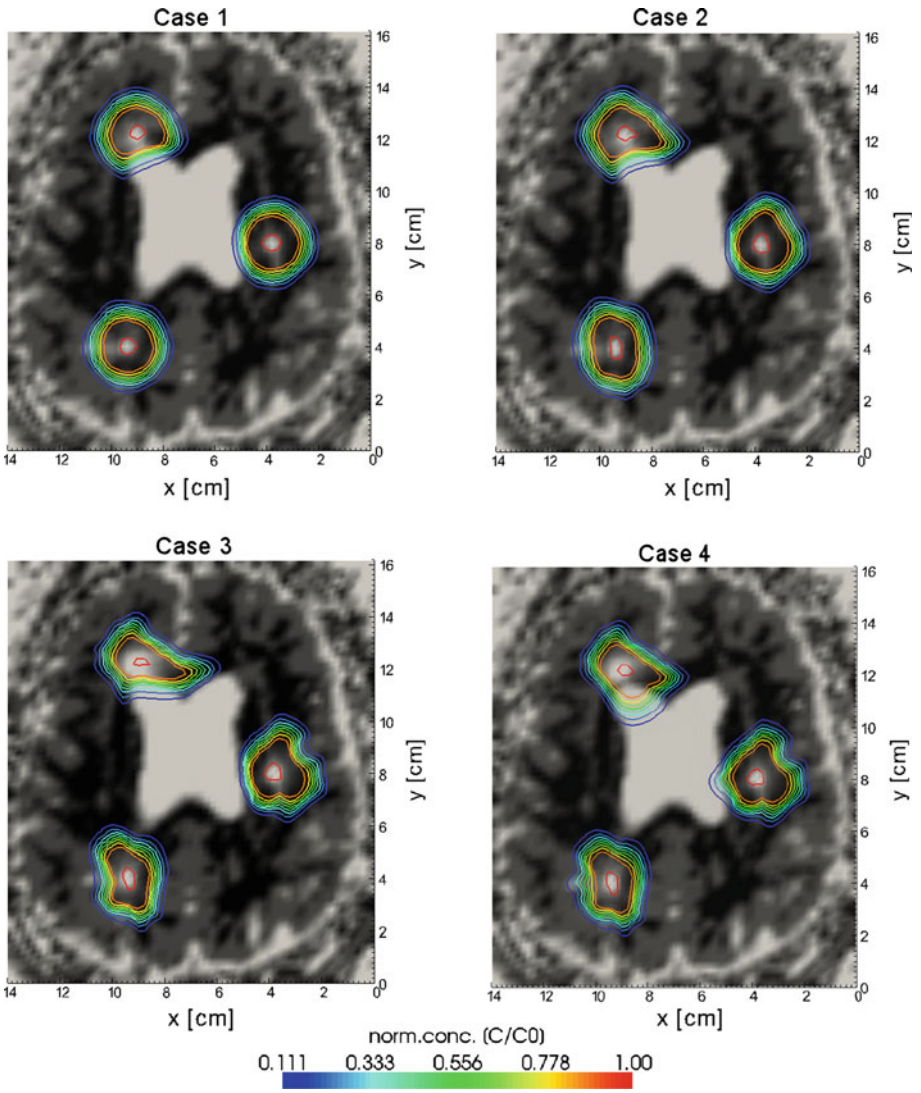

Fig. 10 Distribution of normalized concentration for the four different cases: Case 1: isotropic. Case 2: $\mathbf{K}_0$ equal for both gray and white matter. Case 3: $\mathbf{K}_0$ 10 times higher in the white matter regions than in the gray matter regions. Case 4: a high permeability is assigned to the areas outside the brain tissue

from DTI. FA was used to distinguish between gray and white matters and tortuosity to differentiate between inside and outside the brain tissue. Moreover, the DT-images were used to determine the orientation of the white matter fiber tracts and calibrate the permeability and diffusion tensors. The resolution of the DT-images used here was 2 mm. This is too low to resolve the meningeal layers. To be able to successfully delineate these geometrical boundaries, DT-images with higher resolution will be needed. As can be seen in Sect. 5.1.1, the resolution of the mesh affects all results and a mesh with a finer resolution would yield a better estimation of both pressure and displacement. However, the current

results are qualitatively valuable and demonstrates that, for the concentration distribution to be affected by deformation, the Lamé parameters and/or the permeability must be low. Comparing a rigid model to the poro-elastic model showed the importance of including elasticity in numerical models describing flow and transport during CED. Furthermore, it demonstrated the importance of reliable parameter values. Finally, the parameters obtained from the DT-images were implemented and the effects of anisotropy and heterogeneity were studied. The calibration was shown to be successful and resulted in preferential flow in the direction of the white matter fiber tracts. The next step will be to include non-linear deformation (Smith and Garcia 2011) and to perform simulations with a finer mesh based on DTI data with higher resolution.

Acknowledgments We thank the German Research Foundation (DFG) for the funding within the international Research Training Group "Non-Linearities and Upscaling in Porous Media" (NUPUS). Next we would like to thank Dr. K. Kopitzki and Prof. Dr. J. Voges from Otto-von-Guercke-Universitaet Magdeburg for providing MR-data.

References

Baish, J.W., Netti, P.A., Jain, R.K.: Transmural coupling of fluid flow in microcirculatory network and interstitium in tumors. Microvasc. Res. **53**, 128–141 (1997)

Basser, P.: Interstitial pressure, volume, and flow during infusion into brain tissue. Microvas. Res. **44**, 143–165 (1992)

Basser, P., Pierpaoli, C.: Microstructural and physiological features of tissues elucidated by quantitative-diffusion-tensor mri. J. Magn. Reson. B **111**, 209–219 (1996)

Basser, P., Mattiello, J., Lebihan, D.: Mr diffusion tensor spectroscopy and imaging. Biophys. J. **66**, 259–267 (1994a)

Basser, P., Mattielo, J., Lebihan, D.: Estimation of the effective self-diffusion tensor from the nmr spin-echo. J. Magn. Reson. B **103**, 247–254 (1994b)

Baxter, L., Jain, R.: Transport of fluid and macromolecules in tumors; the role of interstitial pressure and convection. Microvasc. Res. **37**, 77–104 (1989)

Bender, B., Klose, U.: Cerebrospinal fluid and interstitial fluid volume measurements in the human brain at 3t with epi. Magn. Reson. Med. **61**, 834–841 (2009)

Biot, M.: Theory of elasticity and consolidation for a porous anisotropic solid. J. Appl. Phys. **25**, 182–185 (1955)

Bobo, R., Akbasak, D.W.A.L., Morrison, P., Dedrick, R., Oldfield, E.: Convection-enhanced delivery of macromolecules in the brain. Proc. Natl Acad. Sci. USA **91**, 2076–2080 (1994)

Brown, W.: Solid mixture permittivities. J. Chem. Phys. **23**, 1514–1517 (1955)

Chen, X., Sarntinoranont, M.: Biphasic finite element model of solute transport for direct infusion into nervous tissue. Ann. Biomed. Eng. **35**, 2145–2158 (2007)

Chen, Z., Broaddus, W., Viswanathan, R., Raghavan, R., Gillies, G.: Intraparenchymal drug delivery via positive-pressure infusion: Experimental and modeling studies of poroelasticity in brain phantom gels. IEEE Trans. Biomed. Eng. **49**(2), 85–96 (2002)

Cheng, S., Bilston, L.E.: Unconfined compression of white matter. J. Biomech. **40**, 117–124 (2007)

Cheng, S., Clarke, E., Bilston, L.: Rheological properties of the tissues of the central nervous system: a review. Med. Eng. Phys. **30**, 1318–1337 (2008)

Cowin, S., Cardoso, L.: Fabric dependence of wave propagation in anisotropic porous media. Biomech. Model. Mechanobiol. **10**, 39–65 (2011)

Dutta-Roy, T., Wittek, A., Miller, K.: Biomechanical modelling of normal pressure hydrocephalus. J. Biomech. **41**, 2263–2271 (2008)

Flemisch, B., Darcis, M., Erbertseder, K., Faigle, B., Lauser, A., Mosthaf, K., Muthing, S., Nuske, P., Tatomir, A., Wolff, M., Helmig, R.: DuMux: DUNE for multi-{phase, component, scale, physics, ...} flow and transport in porous media. Adv. Water Resour. Corrected Proofs, doi:10.1016/j.advwatres.2011.03.007 (2011)

Garcia, J., Smith, J.: A biphasic hyperelastic model for the analysis of fluid and mass transport in brain tissue. Ann. Biomed. Eng. **37**, 375–386 (2009)

Gillies, G., Smith, J., Humphrey, J., Broaddus, W.: Positive pressure infusion of therapeutic agents into brain tissues: Mathematical and experimental simulations. Technol. Health Care **13**, 235–243 (2005)
Groothuis, R.: The blood-brain and blood-tumor barriers: a review of stragies for increasing drug delivery. Neuro-Oncology **2**, 45–59 (2000)
Hagmann, P., Jonasson, L., Maeder, P., Thiran, J., Wedeen, V., Meuli, R.: Understanding diffusion mr imaging techniques: From scalar diffusion weighted imagin to diffusion tensor imaging and beyond. RadioGraphics **26**, S205–S223 (2006)
Hassanizadeh, M., Gray, W.: General conservation equations for multi phase systems: 3. constitutive theory for porous media flow. Adv. Water Resour. **3**, 25–40 (1980)
Helmig, R.: Multiphase Flow and Transport Processes in the Subsurface. Springer, Heidelberg (1997)
Holz, M., Hei, S., Sacco, A.: Temperature-dependent self-diffusion coefficients of water and six selected molecular liquids for calibration in accurate 1h nmr pfg measurements. Phys. Chem. Chem. Phys. **2**, 4740–4742 (2000)
Kaczmarek, M., Subramaniam, R., Neff, S.: The hydromechanics of hydrocephalus: steady-state solutions for cylindrical geometry. Bull. Math. Biol. **59**(2), 295–323 (1997)
Kalyanasundaram, S., Calhoun, V., Leong, K.: A finite element model for predicting the distribution of drugs intracranially to the brain. Am. J. Physiol. **273**, R1810–R1821 (1997)
Kim, H., Lizak, M., Tansey, G., Csaky, K., Robinson, M., Yuan, P., Wang, N., Lutz, R.: Study of ocular transport of drugs released from an intravitreal implant using magnetic resonance imaging. Ann. Biomed. Eng. **33**(2), 150–164 (2005)
Kim, J., Garett, G., Chen, X., Mareci, T., Sarntinoranont, M.: Voxelized model of interstitial transport in the rat spinal cord following direct infusion into white matter. J. Biomech. Eng. **131**, 071,007 (2009)
Kim, J.H., Mareci, T., Sarntinoranont, M.: A voxelized model of direct infusion into the corpus callosum and hippocampus of the rat brain: model development and parameter analysis. Med. Biol. Eng. Comput. **48**, 203–214 (2010)
Klatt, D., Hamhaber, U., Asbach, P., Braun, J., Sack, I.: Noninvasive assessment of the rheological behavior of human organs using multifrequency mr elastography: a study of brain and liver viscoelasticity. Phys. Med. Biol. **52**, 7281–7294 (2007)
Lai, W., Mow, W.: Drag-induced compression of articular cartilage during a permeation experiment. Biorheology **17**(1–2), 111–123 (1980)
Linninger, A., Somayaji, M., Erickson, T., Guo, X., Penn, R.: Computational methods for predicting drug transport. J. Biomech. **41**, 2176–2178 (2008a)
Linninger, A., Somayaji, M., Mekarsk, M., Zhang, L.: Prediction of convection-enhanced drug delivery to the human brain. J. Theor. Biol. **250**, 125–138 (2008b)
McGuire, S., Zaharoff, D., Yuan, F.: Nonlinear dependence of hydraulic conductivity on tissue deformation during intratumoral infusion. AnnBiomedEng **37**(7), 1173–1181 (2006)
Miller, K., Chinzei, K.: Mechanical properties of brain tissue in tension. J. Biomech. **35**, 483–490 (2002)
Morrison, P.F., Laske, D.W., Bobo, H., Oldfield, E., Dedrick, R.: High-flow microinfusion: tissue penetration and pharmacodynamics. Am. J. Physiol. Regul. Integr. Comp. Physiol. **266**, 292–305 (1994)
Netti, P., Baxter, L., Boucher, Y., Skalak, R., Rakesh, K.: Time-dependent behavior of interstitial fluid pressure in solid tumors: implications for drug delivery. Cancer Res. **55**, 5451–5458 (1995)
Netti, P., Baxter, L., Boucher, Y., Skalak, R., Jain, R.: Macro- and microscopic fluid transport in living tissues: applications to solid tumors. AIChE J. **43**(3), 818–831 (1997)
Nicholson, C.: Diffusion and related transport mechanisms in the brain tissue. Rep. Progr. Phys. **64**, 815–884 (2001)
Odgaard, A.: Three-dimensional methods for quantification of cancellous bone architecture. Bone **20**(4), 315–328 (1997)
Odgaard, A., Kabel, J., van Rietbergen, B., Dalstra, M., Huiskes, R.: Fabric and elastic principal directions of cancellous bone are closely related. J. Biomech. **30**(5), 487–495 (1997)
Prabhu, S., Broaddus, W., Gillies, G., Loudon, W., Chen, Z.J., Smith, B.: Distribution of macromolecular dyes in brain using positivepressure infusion: a model for direct controlled delivery of therapeutic agents. Surg. Neurol. **50**, 367–375 (1998)
Raghavan, R., Brady, M., Rodriguez-Ponze, M., Hartlep, A., Pedain, C., Sampson, J.: Convection-enhanced delivery of therapeutics for brain disease, and its optimization. Neurosurg. Focus **20**(3), E12 (2006)
Sarntinoranont, M., Banerjee, R., Lonser, R., Morrison, P.: A computational model of direct interstitial infusion of macromolecules into spinal cord. Ann. Biomed. Eng. **31**(4), 448–461 (2003)
Sarntinoranont, M., Chen, X., Zhao, J., Mareci, T.: Computational model of interstitial transport in the spinal cord using diffusion tensor imaging. Ann. Biomed. Eng. **34**, 1304–1321 (2006)
Sen, A., Torquato, S.: Effective conductivity of anisotropic two-phase composite media. Phys. Rev. B **39**, 4504–4515 (1988)

Smith, J., Humphrey, A.: Interstitial transport and transvascular fluid exchange during infusion into brain and tumor tissue. Microvasc. Res. **73**, 58–73 (2007)
Smith, J.A., Garcia, J.A.: A nonlinear biphasic model of flow-controlled infusion in brain: fluid transport and tissue deformation analyses. J. Biomech. **42**, 2017–2025 (2009)
Smith, J., Garcia, J.: A nonlinear biphasic model of flow-controlled infusions in brain: mass transport analyses. J. Biomech. **44**, 524–531 (2011)
Taylor, Z., Miller, K.: Reassessment of brain elasticity for analyses of biomechanisms of hydocephalus. J. Biomech. **37**, 1263–1269 (2004)
Tuch, D., Wedeen, V., Dale, A., George, J., Belliveau, J.: Conductivity tensor mapping of the human brain using diffusion tensor mri. Proc. Natl Acad. Sci. **98**, 11697–11701 (2001)
Vorisek, I., Sykova, E.: Measuring diffusion parameters in the brain: comparing the real-time iontophoretic method and diffusion-weighted magnetic resonance. Acta Physiol. **195**, 101–110 (2009)
Zhang, X.Y., Luck, J., Dewhirst, W., Yuan, F.: Interstitial hydraulic conductivity in a fibrosarcoma. Am. J. Physiol. **279**, H2726–H2734 (2000)